

# The $\text{CH}^+$ Abundance in Turbulent, Diffuse Molecular Clouds

Andrew T. Myers<sup>1</sup>, Christopher F. McKee<sup>2,3</sup>, and Pak Shing Li<sup>3</sup>

<sup>1</sup> *Lawrence Berkeley National Laboratory, 1 Cyclotron Road, Berkeley, CA, 94720, USA; atmayers@lbl.gov*

<sup>2</sup> *Department of Physics, University of California, Berkeley, Berkeley, CA 94720*

<sup>3</sup> *Department of Astronomy, University of California, Berkeley, Berkeley, CA 94720*

7 September 2021

## ABSTRACT

The intermittent dissipation of interstellar turbulence is an important energy source in the diffuse ISM. Though on average smaller than the heating rates due to cosmic rays and the photoelectric effect on dust grains, the turbulent cascade can channel large amounts of energy into a relatively small fraction of the gas that consequently undergoes significant heating and chemical enrichment. In particular, this mechanism has been proposed as a solution to the long-standing problem of the high abundance of  $\text{CH}^+$  along diffuse molecular sight lines, which steady-state, low temperature models under-produce by over an order of magnitude. While much work has been done on the structure and chemistry of these small-scale dissipation zones, comparatively little attention has been paid to relating these zones to the properties of the large-scale turbulence. In this paper, we attempt to bridge this gap by estimating the temperature and  $\text{CH}^+$  column density along diffuse molecular sight-lines by post-processing 3-dimensional MHD turbulence simulations. Assuming reasonable values for the cloud density ( $\bar{n}_{\text{H}} = 30 \text{ cm}^{-3}$ ), size ( $L = 20 \text{ pc}$ ), and velocity dispersion ( $\sigma_v = 2.3 \text{ km s}^{-1}$ ), we find that our computed abundances compare well with  $\text{CH}^+$  column density observations, as well as with observations of emission lines from rotationally excited  $\text{H}_2$  molecules.

## 1 INTRODUCTION

The  $\text{CH}^+$  ion is commonly detected along sight lines towards bright O and B stars, with column densities  $\gtrsim 10^{13} \text{ cm}^{-2}$  frequently reported in the literature (e.g. Gredel, van Dishoeck & Black 1993; Gredel 1997; Crane, Lambert & Sheffer 1995; Weselak et al. 2008; Sheffer et al. 2008). This prevalence is puzzling, however, because  $\text{CH}^+$  is destroyed very efficiently by both atomic and molecular hydrogen, and the only reaction that can form  $\text{CH}^+$  rapidly,



is strongly endothermic and can only proceed at temperatures of  $\sim 1000 \text{ K}$  or higher. For this reason, models of diffuse interstellar clouds with  $T \lesssim 100 \text{ K}$ , like those of van Dishoeck & Black (1986), fail dramatically to reproduce these high  $\text{CH}^+$  columns, despite their success with other species.

Most proposed solutions to this problem have invoked

an additional energy source to overcome this 4640 K activation barrier. Possibilities include hydrodynamic (Elitzur & Watson 1978, 1980) and magnetohydrodynamic (Draine & Katz 1986) shock waves, heating in turbulent boundary layers at cloud surfaces (Duley et al. 1992), and particularly dense photon-dominated regions (PDRs) surrounding bright stars (Duley et al. 1992; Sternberg & Dalgarno 1995); for an overview of these mechanisms and some of the problems they face confronting observations, see Gredel (1997). A particularly promising idea, pioneered by Falgarone & Puget (1995), is that the intermittent dissipation of turbulence heats small regions within diffuse clouds to the  $\gtrsim 1000 \text{ K}$  temperatures required for (1) to proceed. Drawing on laboratory experiments of unmagnetized, incompressible turbulent flows, they calculated that if the velocity dispersion in cold, mostly atomic clouds at a scale of  $1 \text{ pc}$  is  $3 \text{ km s}^{-1}$ , then a few percent of the cloud could be heated to  $> 1000 \text{ K}$ , a mass fraction sufficient to bring the  $\text{CH}^+$  abundance in line with observed values (Lambert & Danks 1986). This result was later found to be consistent with magnetized, compressible turbulence simulations as well (Pan & Padoan 2009). These pockets of warm gas may also explain the observed emission from the first few excited rotational states of  $\text{H}_2$  detected in diffuse gas, which is often too large to be explained by UV pumping alone (e.g. Falgarone et al. 2005a; Goldsmith et al. 2010; Ingalls et al. 2011).

Models that rely on turbulent heating alone can over-predict the abundance of other species, such as OH, which is already well modeled by cold cloud models (Federman et al. 1996). However, in addition to the direct heating effect, turbulence can give rise to net drift velocities between the ionic and neutral species in plasmas, enhancing the rates of ion-neutral reactions like (1) beyond those expected from the kinetic temperature alone (e.g. Draine 1980; Flower, Pineau des Forets & Hartquist 1985). Federman et al. (1996) approximated this effect by computing the rate of reaction (1) at the effective temperature  $T_{\text{eff}}$  given by:

$$T_{\text{eff}} = T + \frac{\mu}{3k} v_d^2, \quad (2)$$

where  $\mu$  is the reduced mass of (1) and  $v_d$  is the magnitude of the ion-neutral drift velocity. They proposed that MHD waves with amplitudes  $\sim 3 \text{ km s}^{-1}$  can enhance the predicted column densities of  $\text{CH}^+$  to the observed values even in gas that remains  $T \lesssim 100 \text{ K}$ . A similar calculation was

made in Spaans (1995), who computed the distribution of  $v_d$  from an analytic intermittency model. More recently, Sheffer et al. (2008) included this effect in their PDR models, finding a similar result. The appeal of these models is that they have fewer problems over-producing molecules such as OH, which is not formed by an ion-neutral reaction.

The most successful models include both of these effects simultaneously. Joulain et al. (1998) and Godard, Falgarone & Pineau Des Forêts (2009) treat regions of intense dissipation, termed “Turbulent Dissipation Regions” (TDRs) by Godard, Falgarone & Pineau Des Forêts, as magnetized vortices, taking their (axisymmetric) velocity profiles from that of a Burgers vortex, for which the vorticity as a function of radius is

$$\omega(r) = \omega_0 \exp \left[ - \left( \frac{r}{r_0} \right)^2 \right]. \quad (3)$$

Here,  $\omega_0$  and  $r_0$  are parameters describing the peak vorticity and characteristic fall-off radius in the vortex. Typically,  $\omega_0 \approx 6 \times 10^{-10} \text{ s}^{-1}$  and  $r_0 \approx 40 \text{ AU}$  in Godard, Falgarone & Pineau Des Forêts (2009). These calculations follow the subsequent thermal and chemical evolution of parcels of gas trapped inside such a vortex, including both turbulent heating and ion-neutral drift. Godard, Falgarone & Pineau Des Forêts (2009) then construct models of entire sight lines by assuming they intersect some number of these vortex structures to account for the observed column density of  $\text{CH}^+$ . These models have had a great deal of success reproducing the observed  $\text{CH}^+$  and excited  $\text{H}_2$  columns without over-producing species such as OH.

The goal of this paper is to provide a complementary approach to the above models, which concentrate on individual dissipation events. We post-process the gas temperature  $T$ , drift velocity  $v_d$ , and  $\text{CH}^+$  abundance cell-by-cell through an output of a turbulence simulation from Li et al. (2012) that has been scaled to typical diffuse cloud conditions. This approach loses some of the detail of the above models, but it has the advantage of making fewer simplifying assumptions about, for example, the nature of the intermittent structures or the number of dissipation events along a line of sight. We find that  $\text{CH}^+$  columns in excess of  $\sim 10^{13} \text{ cm}^{-2}$  are readily obtained. We compare our results against a statistically homogenous sample of  $\text{CH}^+$ -containing sight lines from Weselak et al. (2008) and against observations of rotationally excited  $\text{H}_2$ , finding good agreement with both.

## 2 METHODOLOGY

In this section, we provide an overview of our calculation, including our treatment of the heating and cooling rates, the drift velocity, and our calculation of the  $\text{CH}^+$  abundance.

### 2.1 Model Description

The  $\text{CH}^+$  ion is believed to form in partially molecular environments. Indeed, in order for reaction (1) to proceed, at least some of the hydrogen must be in the form of  $\text{H}_2$ , and at least some of the carbon must be in  $\text{C}^+$ . Any plausible formation mechanism is thus not likely to be effective in either the outskirts of molecular clouds with visual extinction  $A_V < 0.1 \text{ mag}$ , where the hydrogen is almost all

**Table 1.** Standard Physical and Chemical Model Parameters

$\bar{n}_{\text{H}}$	$30 \text{ cm}^{-3}$
$L$	$20 \text{ pc}$
$\sigma_{\text{1D}}$	$2.3 \text{ km s}^{-1}$
$\bar{T}_{\text{M}}$	$65 \text{ K}$
$T_{50,\text{M}}$	$35 \text{ K}$
$B_{\text{rms}}$	$5.2 \mu\text{G}$
$x(\text{H})$	$0.68$
$x(\text{H}_2)$	$0.16$
$x(\text{He})$	$0.1$
$x(e^-)$	$1.6 \times 10^{-4}$
$x(\text{C})$	$1.6 \times 10^{-4}$
$x(\text{O})$	$3.2 \times 10^{-4}$

atomic, or deep in their interiors at  $A_V$  greater than a few, where almost all the carbon will be C and/or CO. This gas is sometimes referred to as the “dark gas” since it is difficult to observe (Grenier, Casandjian & Terrier 2005; Wolfire, Hollenbach & McKee 2010).

We therefore model interstellar clouds in which the hydrogen has begun to turn to  $\text{H}_2$ , but the carbon is still primarily in the form of  $\text{C}^+$ . Snow & McCall (2006) classify such clouds as “diffuse molecular clouds.” We treat these regions as cubic boxes with length  $\ell_0$ , mean hydrogen nucleus number density  $\bar{n}_{\text{H}}$ , and one-dimensional velocity dispersion  $\sigma_{\text{1D}}$ . The mean mass per hydrogen nucleus is  $\mu_{\text{H}} = 2.34 \times 10^{-24} \text{ g cm}^{-3}$ . For simplicity, we set the relative abundances (relative to hydrogen nuclei) of molecular hydrogen  $x(\text{H}_2)$  and ionized carbon  $x(\text{C}^+)$  to be constant across the region. For the former, we adopt  $x(\text{H}_2) = 0.16$ , the mean observed molecular fraction from the sample of Weselak et al. (2008), which studied the correlation of  $\text{CH}^+$  column density with that of atomic and molecular hydrogen. For the latter, we take  $x(\text{C}^+) = 1.6 \times 10^{-4}$  from Sofia et al. (2004). Sofia et al. (2011) find using a different measurement technique that the gas-phase carbon abundance is lower than that adopted here by a factor of  $\approx 0.43$ . Since it is not clear which measurement is more accurate, we choose to adopt the higher value. The effects of a lower C abundance in our model are complex. On one hand, it directly reduces the  $\text{CH}^+$  formation rate (see Section 2.5), since  $\text{C}^+$  is one of the reactants in (1). On the other hand, it decreases the cooling rate due to  $\text{C}^+$  (Section 2.3) and increases our estimate for the ion-neutral drift velocity (Section 2.4). The overall effect of decreasing our assumed carbon abundance by a factor of 0.43 is to *increase* the estimate for the  $\text{CH}^+$  abundance by approximately 30%.

Although chemical and physical models of diffuse gas often assume a constant  $n_{\text{H}}$ , the density distribution in the ISM in fact contains a wide range of fluctuations over many orders of magnitude due to the compressive effects of supersonic turbulence. To treat this, we use the results of a  $512^3$  driven, turbulence simulation first published in Li et al. (2012). The density, magnetic field, and velocity at every point in our model are drawn from the corresponding cell in a data dump from this simulation, scaled to physical units by the process described below. A color plot of the column density through the simulation volume is shown in Figure 1. An important caveat to our calculation is that this

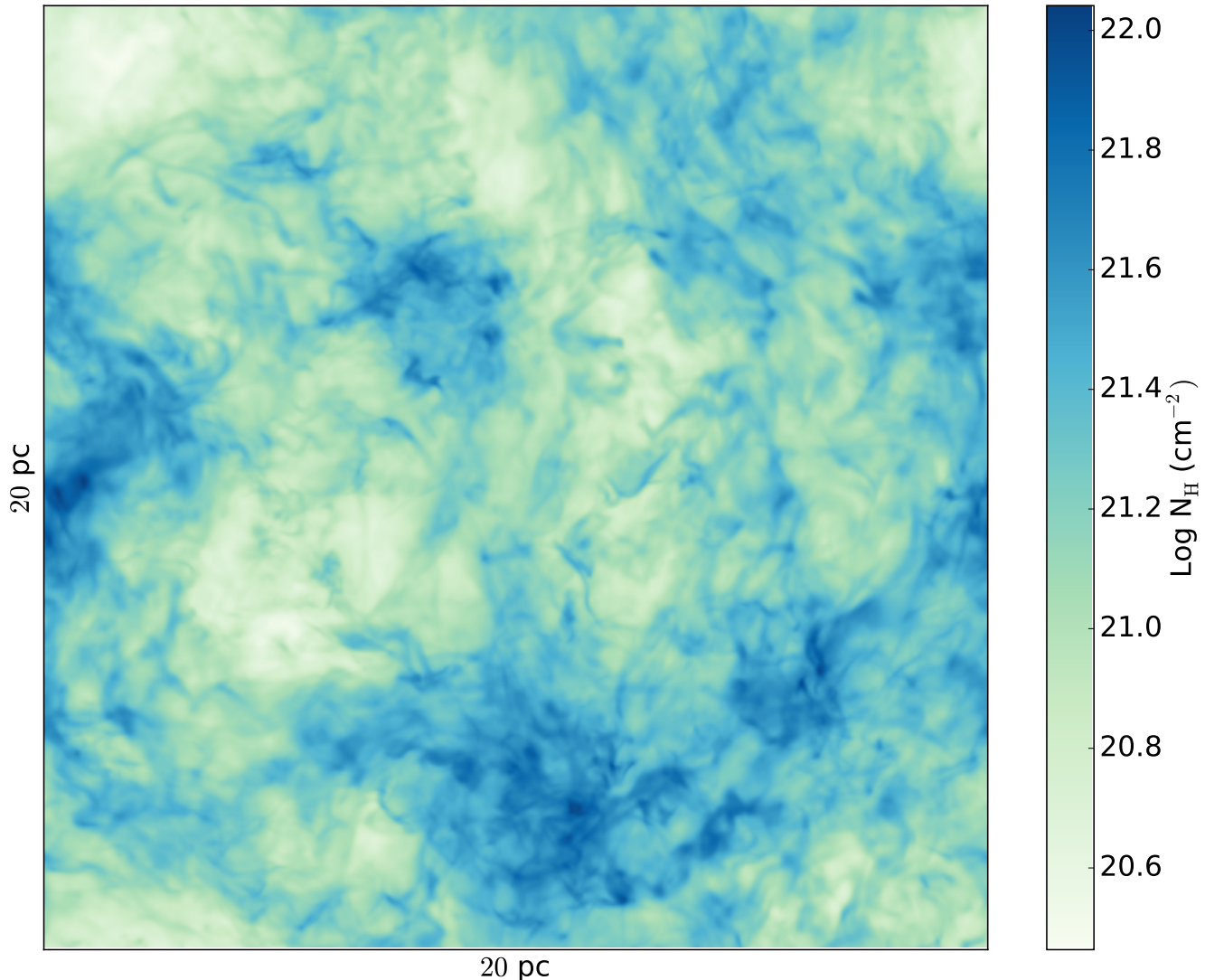


**Figure 1.** Logarithm of the total column density  $N_{\text{H}}$  through the computational domain along the  $x$  direction. The simulation data has been scaled such that the mean  $N_{\text{H}}$  is  $1.83 \times 10^{21} \text{ cm}^{-2}$ . The size of the box is indicated on the  $x$  and  $y$  axes.

simulation data is *isothermal*. We then calculate what the temperature would be if the intermittency in the isothermal case were the same as if the time-dependent heating and cooling effects were followed self-consistently.

## 2.2 Scaling to Physical Units

Simulations of magnetized, isothermal turbulent boxes are characterized by two dimensionless numbers: the 3D sonic Mach number  $\mathcal{M} = \sigma_{3\text{D}}/c_s$  and the 3D Alfvénic Mach number  $\mathcal{M}_A = \sigma_{3\text{D}}/v_A$ . Here,  $\sigma_{3\text{D}}$  is the three-dimensional, density-weighted, non-thermal velocity dispersion in the box,  $c_s = \sqrt{kT/\bar{m}}$  is the isothermal sound speed, where  $T$  is the temperature and  $\bar{m}$  the mean mass per particle, and  $v_A = B_{\text{rms}}/\sqrt{4\pi\bar{\rho}}$  is the Alfvén velocity, where  $B_{\text{rms}}$  is the root-mean-square magnetic field and  $\bar{\rho}$  the mean density. In the simulation considered here, the turbulence was driven so as to maintain  $\mathcal{M} \approx 10$ , and the initial  $\mathcal{M}_A$  was  $\sqrt{5}$ .

In the absence of further constraints, we would be free to scale  $\bar{\rho}$ ,  $\sigma_{3\text{D}}$ ,  $c_s$ ,  $B_{\text{rms}}$  and the size of the box  $\ell_0$  at will as long as the dimensionless ratios  $\mathcal{M}$  and  $\mathcal{M}_A$  remained invariant (see McKee, Li & Klein (2010) for a more rigorous discussion of scaling laws for turbulent box simulations). However, to be consistent with observations of diffuse molecular gas, we impose several additional constraints. First, we require that the gas in the box obey a linewidth-size relation (e.g. McKee & Ostriker 2007):

$$\sigma_{1\text{D}} = \sigma_{\text{pc}} R_{\text{pc}}^{0.5}, \quad (4)$$

where  $R_{\text{pc}}$  is the cloud radius in parsecs, and  $\sigma_{\text{pc}} = 0.72 \text{ km s}^{-1}$ . The 1D non-thermal velocity dispersion  $\sigma_{1\text{D}}$  is related to the 3D value by  $\sigma_{3\text{D}} = \sqrt{3}\sigma_{1\text{D}}$ , and in applying Equation (4), which is meant for approximately spherical clouds, to our cubic simulation domain, we identify the cloud radius  $R$  with  $\ell_0/2$ . Second, we require that the mean column density of hydrogen nuclei be fixed:

$$\bar{N}_{\text{H}} = \bar{n}_{\text{H}}\ell_0 = \bar{N}_{\text{obs}}, \quad (5)$$

where  $\bar{N}_{\text{obs}} \approx 1.83 \times 10^{21} \text{ cm}^{-2}$  is the mean total column density from Weselak et al. (2008). This column corresponds to  $A_V \approx 1$ , consistent with our requirement that the gas be partially molecular. Note that Equations (4) and (5) imply that we cannot independently choose  $n_{\text{H}}$ ,  $\ell_0$  and  $\sigma_{1\text{D}}$ ; choosing a density fixes the box size  $\ell_0$ , which fixes the velocity dispersion through the linewidth-size relation. Numerically:

$$\begin{aligned} \ell_0 &\approx 19.8 \left( \frac{30 \text{ cm}^{-3}}{\bar{n}_{\text{H}}} \right) \text{ pc}, \\ \sigma_{1\text{D}} &\approx 2.3 \left( \frac{30 \text{ cm}^{-3}}{\bar{n}_{\text{H}}} \right)^{0.5} \text{ km s}^{-1}. \end{aligned} \quad (6)$$

The dynamical timescale in our model can thus be estimated as:

$$t_{\text{dyn}} = \frac{\ell_0}{\sigma_{1\text{D}}} \approx 8.5 \times 10^6 \left( \frac{30 \text{ cm}^{-3}}{\bar{n}_{\text{H}}} \right)^{0.5} \text{ yr}. \quad (7)$$

We assume that properties of the fluid flow (the density, velocity, and magnetic field) change on this timescale. We show that this is large compared to the thermal and chemical timescales below.

These relations also fix (along with the fact the  $\mathcal{M}_{\Lambda} = 2.2$ ) the rms magnetic field strength in the box:

$$B_{\text{rms}} = \sqrt{\frac{6\pi\mu_{\text{H}}\bar{N}_{\text{obs}}\sigma_{\text{pc}}^2}{(1 \text{ pc})\mathcal{M}_{\Lambda}^2}} \approx 5.3 \mu\text{G}. \quad (8)$$

Crutcher et al. (2010) infer that interstellar fields in gas with  $\bar{n}_{\text{H}} \lesssim 300 \text{ cm}^{-3}$  are uniformly distributed in strength between very low values and  $10 \mu\text{G}$ , so this field is quite typical. Note that only one of  $\bar{n}_{\text{H}}$ ,  $\ell_0$ ,  $\sigma_{3\text{D}}$ , and  $B_{\text{rms}}$  may be set independently, with the others following from that choice.

The final remaining dimensional parameter describing our turbulence simulation is the isothermal sound speed  $c_s$ . The sound speed of a gas with  $x(\text{H}_2) = 0.16$  and  $x(\text{He}) = 0.1$  is

$$c_s(T) \approx 0.74 \sqrt{\frac{T}{100 \text{ K}}} \text{ km s}^{-1}. \quad (9)$$

However, because the temperature is an output of our model, we cannot set it arbitrarily. We thus compute the temperature using the process described below for a range of boxes, each scaled to a different  $\bar{n}_{\text{H}}$ , and select the one for which  $\mathcal{M}$  computed using the mass-weighted median temperature  $T_{50,\text{M}}$  (the  $T$  for which half of the mass in cloud is hotter) is  $\approx 10$ . We find that this occurs at  $n_{\text{H}} \approx 30 \text{ cm}^{-3}$  and adopt that as our fiducial density. This is the same value adopted in the standard model of Joulain et al. (1998). However, individual sight lines passing through the simulation volume can have mean densities ranging from  $\approx 5 \text{ cm}^{-3}$  to  $\approx 180 \text{ cm}^{-3}$ . The corresponding  $T_{50,\text{M}}$  is  $\approx 35 \text{ K}$ , and the mass-weighted mean temperature is  $\bar{T}_{\text{M}} \approx 65 \text{ K}$ . We summarize the physical and chemical parameters describing this model in Table 1.

Our simulation data does not include the effects of self-gravity. As a consistency check, we compute the virial parameter  $\alpha_{\text{vir}}$  to verify that turbulence indeed dominates self-gravity. Using the above parameters, the total mass  $M$  in the box is  $\approx 8000 M_{\odot}$ . The virial parameter for a spherical cloud of mass  $M$  and radius  $R$  is  $\alpha_{\text{vir}} = 5\sigma_{1\text{D}}^2 R/GM$  (Bertoldi & McKee 1992). Using  $R = \ell_0/2$ , we find  $\alpha_{\text{vir}} \approx 7.4$ , which is

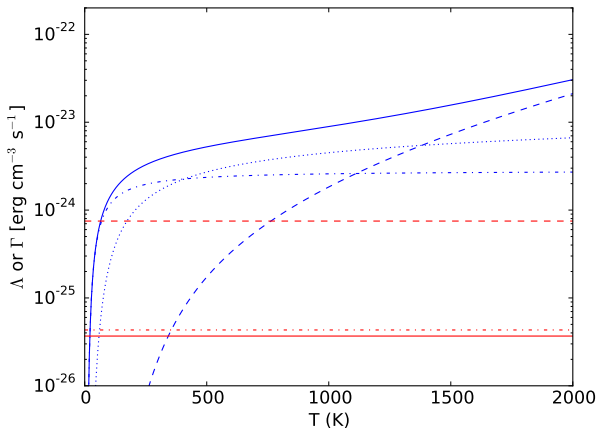


**Figure 2.** Heating (red) and cooling (blue) rates per unit volume versus  $T$  for  $n_{\text{H}} = 30 \text{ cm}^{-3}$  and the standard chemical abundances shown in Table 1. The solid blue curve shows  $n_{\text{H}}\Lambda_{\text{tot}}$ , while the dashed, dashed-dotted, and dotted curves are  $n_{\text{H}}\Lambda_{\text{H}_2}$ ,  $n_{\text{H}}\Lambda_{\text{C}^+}$ , and  $n_{\text{H}}\Lambda_{\text{O}}$ , respectively. The solid, dashed, and dashed-dotted red lines show the mean values of  $\Gamma_{\text{Turb}}$ ,  $\Gamma_{\text{PE}}$ , and  $\Gamma_{\text{CR}}$ , respectively.

large enough that the effects of self-gravity are indeed negligible. We can also characterize the relative importance of gravity and magnetic fields in the box by computing the mass-to-flux ratio relative to critical,  $\mu_{\Phi} \equiv M/M_{\Phi}$ , where  $M_{\Phi} \approx \Phi/2\pi\sqrt{G}$  and  $\Phi$  is the magnetic flux threading the cloud. For our adopted parameters,  $\mu_{\Phi} \approx 1.3$ , so the cloud is marginally magnetically supercritical.

### 2.3 Heating and Cooling

The temperature in each cell is set by a balance between heating and cooling:

$$\Gamma_{\text{Turb}} + \Gamma_{\text{CR}} + \Gamma_{\text{PE}} = n_{\text{H}}\Lambda_{\text{tot}}(T). \quad (10)$$

where  $\Gamma_{\text{Turb}}$ ,  $\Gamma_{\text{CR}}$ , and  $\Gamma_{\text{PE}}$  are the heating rates per unit volume due to the dissipation of turbulence, cosmic ray ionizations, and the photoelectric effect on dust grains, respectively.  $n_{\text{H}}\Lambda_{\text{tot}}(T)$  is the total cooling rate per unit volume, which we assume is dominated by electronic transitions of  $\text{C}^+$  and  $\text{O}$  and by ro-vibrational transitions of the  $\text{H}_2$  molecule. Note that throughout this paper, we use  $\lambda$  to represent the cooling rate *coefficient* ( $\text{erg cm}^3 \text{ s}^{-1}$ ) and  $\Lambda$  for the cooling rate per H nucleus ( $\text{erg s}^{-1}$ ).

$\Gamma_{\text{CR}}$  can be expressed as the product of three factors - the total cosmic ray ionization rate per H nucleus  $\zeta_{\text{H}}$  (including both primary and secondary ionizations), the average energy deposited into the medium per ionization  $\Delta Q$ , and  $n_{\text{H}}$ . Both  $\zeta_{\text{H}}$  and  $\Delta Q$  are rather uncertain and can vary considerably over different Galactic environments. Typical values of  $\zeta_{\text{H}}$  in dense gas are  $\sim 1 - 5 \times 10^{-17} \text{ s}^{-1}$  (Dalgarno 2006), but there is evidence from  $\text{H}_3^+$  observations that  $\zeta_{\text{H}}$  is considerably higher in the diffuse gas under consideration here (Dalgarno 2006; Indriolo & McCall 2012). Indriolo & McCall (2012) find a mean  $\zeta_{\text{H}}$  of  $1.8 \times 10^{-16} \text{ s}^{-1}$  in their sample of diffuse molecular sight lines, and values as large as  $\sim 1 \times 10^{-15} \text{ s}^{-1}$  have been reported in the literature (Snow & McCall 2006; Shaw et al. 2008). In this paper, we adopt the value  $1.8 \times 10^{-16} \text{ s}^{-1}$ . For  $\Delta Q$ , we use 10 eV, as

estimated for diffuse molecular gas from Table 6 of Glassgold, Galli & Padovani (2012), although it is important to note that this value can vary by several eV depending on the precise physical and chemical conditions in the cloud. Combining these factors, the cosmic ray heating rate is:

$$\begin{aligned} \Gamma_{\text{CR}} &= \zeta \Delta Q n_{\text{H}} \\ &\approx 1.9 \times 10^{-25} \left( \frac{n_{\text{H}}}{30 \text{ cm}^{-3}} \right) \text{ ergs cm}^{-3} \text{ s}^{-1} \end{aligned} \quad (11)$$

For  $\Gamma_{\text{PE}}$ , we adopt the expression:

$$\Gamma_{\text{PE}} = 1.3 \times 10^{-24} n_{\text{H}} \epsilon G_0 \text{ ergs cm}^{-3} \text{ s}^{-1} \quad (12)$$

from Wolfire et al. (2003), where  $G_0$  is the intensity of FUV light in units of the Habing (1968) field and  $\epsilon$  is a heating efficiency factor given by Equation (20) of Wolfire et al. (2003). For  $n_{\text{H}} = 30 \text{ cm}^{-3}$ ,  $T = 100 \text{ K}$ , an electron fraction of  $1.6 \times 10^{-4}$ , and a FUV field of  $G_0 = 1.1$  (Mathis, Mezger & Panagia 1983),  $\epsilon$  evaluates to  $1.8 \times 10^{-2}$ , yielding

$$\Gamma_{\text{PE}} = 7.6 \times 10^{-25} \left( \frac{n_{\text{H}}}{30 \text{ cm}^{-3}} \right) \text{ ergs cm}^{-3} \text{ s}^{-1} \quad (13)$$

The final heating process we consider is  $\Gamma_{\text{Turb}}$ . Dimensional arguments (e.g. Landau & Lifshitz 1959) and numerical simulations (e.g. Stone, Ostriker & Gammie 1998; Mac Low 1999) both suggest that the kinetic energy in a turbulent cloud  $1/2 \rho \sigma_{3\text{D}}^2$  decays in roughly one crossing time  $\ell_0/\sigma_{3\text{D}}$ , so that the volume-averaged turbulent heating rate is approximately

$$\begin{aligned} \bar{\Gamma}_{\text{Turb}} &\approx \frac{1}{2} \frac{\rho \sigma_{3\text{D}}^3}{\ell_0} \\ &\approx 3.5 \times 10^{-26} \sqrt{\frac{n_{\text{H}}}{30 \text{ cm}^{-3}}} \text{ ergs cm}^{-3} \text{ s}^{-1}, \end{aligned} \quad (14)$$

where in the last step we have assumed the scaling given by Equations (4) and (5). Locally, however,  $\Gamma_{\text{Turb}}$  exhibits large fluctuations from place to place, a phenomenon known as intermittency. To calculate the spatial dependence of  $\Gamma_{\text{Turb}}$ , we follow the calculation in Pan & Padoan (2009). To summarize their argument, the work done against the viscous forces in a fluid with velocity field  $\mathbf{v}$  is irreversibly converted into heat at rate per unit volume given by:

$$\Gamma_{\text{Turb}}(\mathbf{x}) = \frac{1}{2} \rho \nu \left( \partial_i v_j + \partial_j v_i - \frac{2}{3} (\nabla \cdot \mathbf{v}) \delta_{ij} \right)^2. \quad (15)$$

This rate depends on the kinematic viscosity of the fluid,  $\nu$ . However, in our simulations, which were based on the Euler equations for a compressible gas, the viscosity was numerical in origin, and thus does not have its true microphysical value. Instead, we treat  $\nu$  as a proportionality constant that takes whatever value is required so that the volume average of Equation (15) equals Equation (14). Once this constant has been determined, we can compute  $\Gamma_{\text{Turb}}(\mathbf{x})$  for each cell in the simulation.

Note that the resolution of our simulation data  $\Delta x = \ell_0/512 \approx 8 \times 10^3 \text{ AU}$  is significantly larger than the dissipation scale provided by the kinematic viscosity of interstellar gas of  $\ell_d \sim 10 \text{ AU}$  (Joulain et al. 1998). If the turbulence were allowed to cascade down to these small scales, the distribution of the heating rate would be more intermittent than it is in our simulation (Pan & Padoan 2009). However, viscous dissipation is not the only process that removes

energy from the turbulent cascade. Ion-neutral friction becomes significant at the much larger scale  $\ell_{\text{AD}}$  (see Section 2.4), and is capable of dissipating most ( $\approx 70 \%$  for  $\mathcal{M}_A \approx 1$ ) of the energy in the cascade at scales  $\approx 10 \ell_{\text{AD}}$  (Li, Myers & McKee 2012), which is comparable to the cell size in our numerical data. Below  $\ell_{\text{AD}}$ , a turbulent cascade can re-assert itself in the neutrals, allowing some of the energy to be dissipated on the  $\sim 10 \text{ AU}$  scale set by viscosity. While our procedure likely under-estimates the intermittency for this remaining  $\approx 30 \%$  of the energy, it is more accurate than the opposite assumption that all the energy in cascade makes it to  $\sim 10 \text{ AU}$  scales. Note that this procedure for estimating the turbulent heating rate is scaled such that it includes *all* the energy removed from the turbulent cascade by dissipative processes, whether the physical mechanism is molecular viscosity or ambipolar diffusion. We do not separately include an ambipolar diffusion heating term in Equation (10) because doing so would amount to double counting.

For the  $\text{C}^+$  and O cooling coefficients, we adopt the formulas given by Wolfire et al. (2003):

$$\begin{aligned} \lambda_{\text{C}^+}(T) &= 3.6 \times 10^{-27} \exp(-92 \text{ K}/T) \text{ erg cm}^3 \text{ s}^{-1} \\ \lambda_{\text{O}}(T) &= 2.35 \times 10^{-27} \left( \frac{T}{100 \text{ K}} \right)^{0.4} \\ &\quad \times \exp(-228 \text{ K}/T) \text{ erg cm}^3 \text{ s}^{-1}, \end{aligned} \quad (16)$$

where we have scaled the overall numerical factors to account for our fractional abundances of carbon and oxygen of  $1.6 \times 10^{-4}$  and  $3.2 \times 10^{-4}$ , rather than the  $1.4 \times 10^{-4}$  and  $3.4 \times 10^{-4}$  used in Wolfire et al. (2003). The cooling rates per H nucleus are then  $\Lambda_{\text{C}^+}(T) = n_{\text{H}} \lambda_{\text{C}^+}(T)$  and  $\Lambda_{\text{O}}(T) = n_{\text{H}} \lambda_{\text{O}}(T)$ . These rates are valid for  $n_{\text{H}} < n_{\text{crit}} \simeq 3000 \text{ cm}^{-3}$ .

The final thermal process we consider is the cooling rate due to the  $\text{H}_2$  molecule. This coolant is particularly important in the warm (over a few hundred K) gas in which  $\text{CH}^+$  is expected to form. In the low density limit, the  $\text{H}_2$  level populations are sub-thermal and the cooling rate  $\Lambda_{\text{H}_2}(n_{\text{H}} \rightarrow 0)(T)$  is a sum over the rates due to collisions with H,  $\text{H}_2$ , He, and e. For these rates, we use the tables in Glover & Abel (2008), assuming an ortho:para ratio of 0.7 (see section 3.3) and the fractional abundances of H,  $\text{H}_2$ , He and electrons listed in Table 1. These rates are valid at arbitrarily low gas densities, since the cooling rate coefficients themselves are independent of the gas density in this limit. At densities high enough for local thermodynamic equilibrium to be established, the  $\text{H}_2$  cooling rate per H nucleus  $\Lambda_{\text{H}_2, \text{LTE}}(T)$  becomes independent of the collision partner abundances, and we adopt the cooling rate from Coppola et al. (2012). We bridge these two limits following Hollenbach & McKee (1979):

$$\Lambda_{\text{H}_2}(T) = \frac{\Lambda_{\text{H}_2, \text{LTE}}(T)}{1 + \Lambda_{\text{H}_2, \text{LTE}}(T)/\Lambda_{\text{H}_2}(n_{\text{H}} \rightarrow 0)(T)} \quad (17)$$

The total cooling rate is then

$$\Lambda_{\text{tot}}(T) = \Lambda_{\text{C}^+}(T) + \Lambda_{\text{O}}(T) + x_{\text{H}_2} \Lambda_{\text{H}_2}(T). \quad (18)$$

Equation (10) becomes a non-linear equation for  $T$  in each cell, which we solve numerically using the `scipy.optimize.brent` routine from the SciPy software library (Jones et al. 2001–). The magnitudes of these cooling processes are summarized as a function of temperature in Figure 2 for our standard model parameters. For compari-

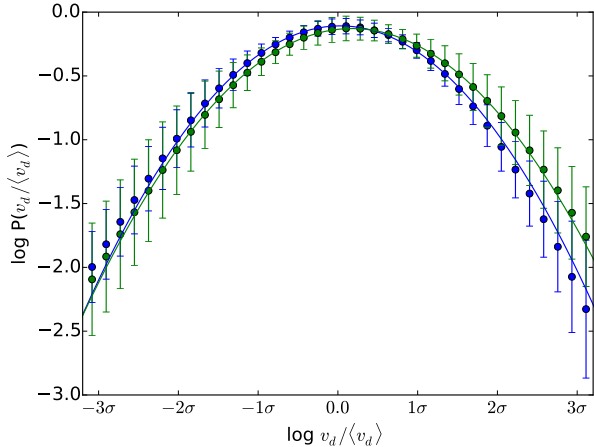


**Figure 3.** Blue - the circles show the mass-weighted distribution of  $v_d$  divided by its mean value  $\langle v_d \rangle$  from the  $\mathcal{M} = 3$ ,  $\mathcal{M}_A = 0.67$ ,  $R_{AD}(\ell_0) \approx 1000$  AD simulation. The error bars show the  $2\sigma$  temporal variation in distribution over 2 box crossing times, and solid line shows the best-fit log-normal. Green - same, but for the  $\mathcal{M} = 3$ ,  $\mathcal{M}_A = 0.67$  ideal simulation, with  $v_d$  computed from Equation (22). The agreement between the two curves is quite good over more than 3 standard deviations.

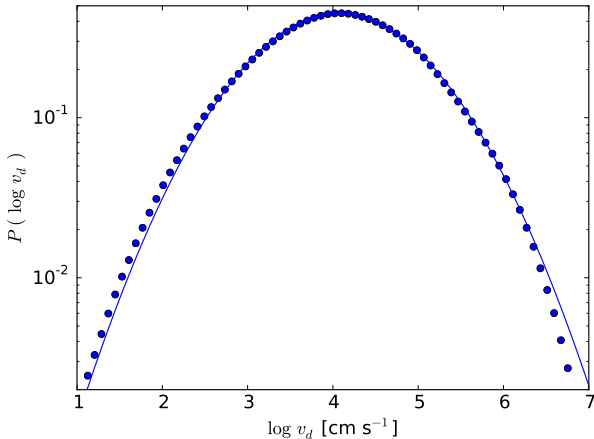


**Figure 4.** Distribution of  $\log v_d$  for our model in physical units. The blue circles are the simulation data, and the solid line is a best-fit normal distribution with a mean of 4.04 and a standard deviation of 0.89.

son, the (constant) values of the various heating rates are also displayed for our standard density of  $n_H = 30 \text{ cm}^{-3}$ .

We estimate the typical cooling time in our model as the thermal energy density divided by the cooling rate:

$$t_{\text{cool}} = \frac{3/2kT}{\Lambda_{\text{tot}}(T)} \simeq 3.3 \times 10^4 \text{ yr}, \quad (19)$$

where the numerical evaluation is for our fiducial values of  $n_H = 30 \text{ cm}^{-3}$  and  $T_{50,M} = 35 \text{ K}$ . This is two orders of magnitude smaller than the dynamical time (Equation (7)), which justifies our use of an energy balance equation.

## 2.4 Ion-Neutral Drift

In the presence of ambipolar diffusion (the net slippage between the charged and neutral species in a plasma), ion-neutral reactions like (1) can proceed at rates faster than those expected from the kinetic temperature alone (e.g. Draine 1980; Flower, Pineau des Forets & Hartquist 1985). The relative importance of the ambipolar and inertial forces in a turbulent system can be characterized by the ambipolar diffusion Reynolds number  $R_{AD}(\ell_0)$  (Zweibel & Brandenburg 1997; Li, Myers & McKee 2012):

$$R_{AD}(\ell_0) \equiv \frac{4\pi\gamma_{AD}\rho_i\rho_n\ell_0\sigma_{3D}}{B_{\text{rms}}^2}, \quad (20)$$

where  $\rho_i$  and  $\rho_n$  are the densities of the ionic and neutral components of the fluid and  $\gamma_{AD}$  is the ion-neutral coupling constant given by  $\langle \sigma v \rangle / (m_i + m_n)$ . For  $\text{C}^+$  and  $\text{H}_2$ , this evaluates to  $8.47 \times 10^{13} \text{ cm}^3 \text{ s}^{-1} \text{ g}^{-1}$  (Draine 1980). Applying Equations (4) and (5) for our adopted degree of ionization and magnetic field strength,  $R_{AD}(\ell_0)$  is

$$R_{AD}(\ell_0) \approx 6.3 \times 10^3 \sqrt{\left(\frac{n_H}{30 \text{ cm}^{-3}}\right)} \gg 1. \quad (21)$$

The corresponding length scale  $\ell_{AD} = \ell_0 / R_{AD}(\ell_0)$  at which ambipolar dissipation becomes significant is  $\approx 640 \text{ AU}$  for  $n_H = 30 \text{ cm}^{-3}$ . Thus, ambipolar drift should not be significant on large scales in our model. However, as with the turbulent heating rate, there may be isolated regions in the tails of the drift velocity distribution where this effect is significant.

To proceed, we need a prescription for computing  $v_d$ . Unfortunately, two-fluid simulations of MHD turbulence are prohibitively expensive in the high  $\mathcal{M}$ , strongly coupled regime considered here. To estimate the effects of  $v_d$  on the production of  $\text{CH}^+$ , we instead use our ideal MHD data along with an approximate analytic expression for the drift velocity in the strongly coupled regime, which we corroborate with direct numerical simulations of turbulent ambipolar diffusion at lower  $\mathcal{M}$ . Specifically, if the system is weakly ionized, then the Lorentz force and the ion-neutral drag force dominate all the other terms in the ion momentum equation and the drift is given by  $v_d = |(\vec{\nabla} \times \vec{B}) \times \vec{B}| / 4\pi\gamma_{AD}\rho_i\rho_n$  (e.g. Shu 1992). If the effects of ambipolar diffusion are weak enough that they have only a minor effect on the geometry of the magnetic field, we can estimate the drift by computing  $|(\vec{\nabla} \times \vec{B}) \times \vec{B}|$  in the ideal limit:

$$v_d \approx \frac{|(\vec{\nabla} \times \vec{B}) \times \vec{B}|^{\text{Ideal}}}{4\pi\gamma_{AD}\rho_i\rho_n}. \quad (22)$$

This procedure is illustrated in Figure 3. We take two simulations of  $\mathcal{M} = 3$ ,  $\mathcal{M}_A = 0.67$  turbulence from Li et al. (2008), one which follows the ion and neutral fluids separately, and one which assumes ideal MHD. The AD simulation has  $R_{AD}(\ell_0) \approx 1000$ . We directly compute the time-averaged, density-weighted distribution of  $v_d$  in the non-ideal simulation, and compare it to that of Equation (22) computed using the ideal data with  $\gamma_{AD}$  and  $\chi_i$  chosen to match the AD simulation. The resulting distributions both have an approximately log-normal form:

$$P(\log v_d) d \log v_d = \frac{1}{\sigma_{\log v_d} \sqrt{2\pi}} \exp\left(-\frac{(\log v_d - \mu_{\log v_d})^2}{2\sigma_{\log v_d}^2}\right) \quad (23)$$

and agree with each other to within the error bars, which show the magnitude of the temporal fluctuation in the drift distribution computed over 2 crossing times. Equation (22) does slightly over-predict the simulated value of  $v_d$ : both the mean  $\mu_{\log v_d}$  and standard deviation  $\sigma_{\log v_d}$  of the Lorentz drift approximation are larger than those of the log-normal fit to the true drift distribution by 5% and 2%, respectively. This is likely because, although  $R_{\text{AD}}(\ell_0)$  for the entire box is  $\sim 1000$ , there are still sub-regions in the box where the coupling is less strong. We expect that this approximation should improve with increasing  $R_{\text{AD}}(\ell_0)$ .

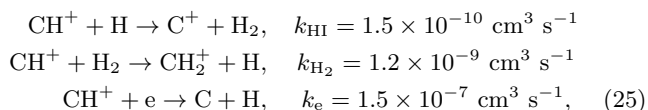
Figure 4 shows the result of applying this procedure to our  $\mathcal{M} \approx 10$ ,  $\mathcal{M}_A \approx 2.2$  Ideal MHD data, scaled to physical units as described above. Here, we again find that the distribution of  $\log(v_d)$  is approximately normal, with best-fit parameters  $\mu_{\log v_d} = 4.04$  and  $\sigma_{\log v_d} = 0.89$ . Although the error in the best-fit lognormal parameters found above is small, it could potentially have a large impact on the  $\text{CH}^+$  abundance, since that is primarily determined by the tails of the distribution. We can estimate the accuracy of our approximation as follows. First, we compute the mean  $\text{CH}^+$  abundance (see Section 2.5 below) in a cloud with constant density  $n_{\text{H}} = 30 \text{ cm}^{-3}$  and kinetic temperature  $T = 35 \text{ K}$  using Equations (26) and (2), under the assumption that the distribution of  $v_d$  is given by Equation (23) with our best fit parameters. We then recompute the  $\text{CH}^+$  abundance using values of  $\mu_{\log v_d}$  and  $\sigma_{\log v_d}$  that are lower by 5% and 2%, respectively - the error we found for the  $\mathcal{M} = 3$ ,  $\mathcal{M}_A = 0.67$  case above. The result is that the two abundances agree to within a factor of 2. As the  $R_{\text{AD}}(\ell_0)$  in our target system is larger than 1000 (Equation 21), we expect the true error to be somewhat less than this.

## 2.5 Chemistry

To assess the viability of turbulent dissipation as an energy source for  $\text{CH}^+$  production, we perform a simple analytic estimate of the  $\text{CH}^+$  abundance in a cell as a function of  $n_{\text{H}}$  and  $T_{\text{eff}}$  following Lambert & Danks (1986).  $\text{CH}^+$  forms through reaction 1 with a rate constant:

$$k_f = 1.5 \times 10^{-10} \times \exp(-4640 \text{ K}/T_{\text{eff}}). \quad (24)$$

Once it forms, it will be quickly destroyed by reactions with  $\text{H}$ ,  $\text{H}_2$ , and electrons. The rates for these processes are



where we have adopted the values used by the Meudon PDR code<sup>1</sup>.

Because the electron fraction  $x_e \approx x_i$  is  $\sim 10^{-4}$ , removal of  $\text{CH}^+$  by electrons is not crucial and we ignore it in our calculations. However, destruction by atomic and molecular hydrogen are both important. Balancing the rate of formation with the rate of destruction  $n_{\text{C}^+} n_{\text{H}_2} k_f =$

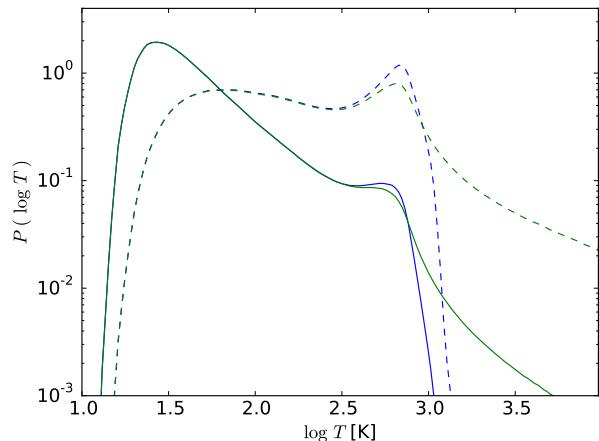


**Figure 5.** Blue solid line - mass-weighted differential distribution function of  $\log T$ . Green solid line - the volume-weighted distribution of same. Dotted lines - the colors have the same meaning as before, but the distribution of  $\log T_{\text{eff}}$  has been plotted instead.

$n_{\text{CH}^+} n_{\text{HI}} k_{\text{HI}} + n_{\text{CH}^+} n_{\text{H}_2} k_{\text{H}_2}$ , we can derive

$$\begin{aligned} n_{\text{CH}^+} &= x(\text{C}^+) \frac{x(\text{H}_2)}{1-2x(\text{H}_2)} \frac{k_f}{k_{\text{HI}}} \left( 1 + \frac{k_{\text{H}_2}}{k_{\text{HI}}} \frac{x(\text{H}_2)}{1-2x(\text{H}_2)} \right)^{-1} n_{\text{H}} \\ &\approx 3.9 \times 10^{-4} \left( \frac{n_{\text{H}}}{30 \text{ cm}^{-3}} \right) \times \exp\left( \frac{-4640 \text{ K}}{T_{\text{eff}}} \right). \end{aligned} \quad (26)$$

Equation 26 highlights the importance of both the molecular fraction and the  $\text{C}^+$  abundance for  $\text{CH}^+$  production; the gas must be well-shielded enough from the ambient radiation field that some of the hydrogen is molecular form, but not so well-shielded that carbon is all molecular.

We can also estimate a typical  $\text{CH}^+$  formation timescale as follows. Suppose we are in a region that initially contains no  $\text{CH}^+$  that is subsequently subject to heating. From reaction 25, the rate of change in  $n_{\text{CH}^+}$  is

$$\frac{dn_{\text{CH}^+}}{dt} = n_{\text{C}^+} n_{\text{H}_2} k_f - n_{\text{CH}^+} n_{\text{HI}} k_{\text{HI}} - n_{\text{CH}^+} n_{\text{H}_2} k_{\text{H}_2}. \quad (27)$$

The solution to this equation is

$$n_{\text{CH}^+}(t) = n_{\text{CH}^+, \text{eq}} \times [1 - \exp(-at)], \quad (28)$$

where  $n_{\text{CH}^+, \text{eq}}$  is the equilibrium abundance given by Equation 26 and  $a = (1-2x_{\text{H}_2})k_{\text{HI}} + x_{\text{H}_2}k_{\text{H}_2}$ . Thus, the time over which the  $\text{CH}^+$  abundance achieves 90% of its equilibrium value is

$$t_{\text{CH}^+} = \frac{\ln(10)}{a} \approx 250 \text{ yr}. \quad (29)$$

This is 2 orders of magnitude shorter than the cooling time (Equation 19), and 4 orders shorter than the characteristic dynamical time (Equation 7).

## 3 RESULTS

### 3.1 Temperature and $\text{CH}^+$ Abundance

The result of our temperature calculation is summarized in Figures 5 and 6. Figure 5 shows the mass- and volume-weighted differential probability distribution functions of  $\log T$  and  $\log T_{\text{eff}}$ . Figure 6 shows the cumulative distribution functions of the same quantities. Both  $T$  and  $T_{\text{eff}}$  can take a large range of values spanning over 3 orders of

<sup>1</sup> <http://pdr.obspm.fr/PDRcode.html>

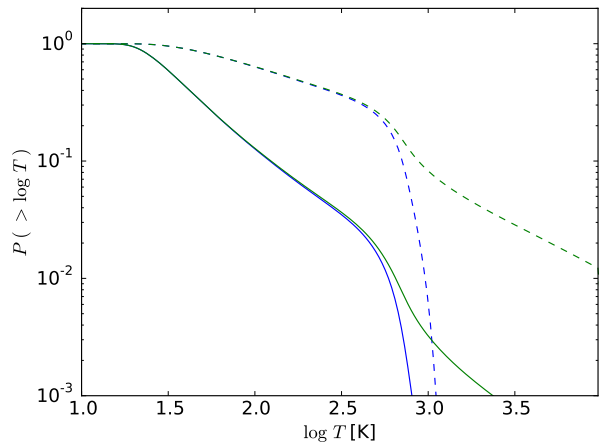


**Figure 6.** Same as Figure 5, but showing the cumulative rather than the differential distribution functions. Specifically,  $P(> \log T)$  shows the fraction of the mass or volume with values of  $\log T$  greater than the corresponding value on the x-axis. As before, the solid lines show the distribution of  $\log T$  and the dotted lines the distribution of  $\log T_{\text{eff}}$ .

magnitude. The distributions of both quantities appear to be bimodal, showing peaks at several tens and several hundreds of K. The large majority of the mass lies at low  $T$ , but a small fraction is found in high temperature “pockets” - precisely the arrangement proposed by Falgarone & Puget (1995). An interesting feature of these distributions is the importance of density variations in setting the temperature. The difference between the mass- and volume weighted distributions shows that high values of  $T$  and  $T_{\text{eff}}$  tend to be found in relatively low-density gas. This is easily understood from Equations (10) and (22). From Equation (10), the heating processes are all proportional to  $n_{\text{H}}$ . Furthermore, at low  $T$ , the dominant cooling processes are  $\text{C}^+$  and O lines, for which the cooling power goes like  $n_{\text{H}}^2$ . Accordingly, cooling can balance heating at relatively low temperatures unless  $n_{\text{H}}$  is small. Similarly, the drift velocity  $v_d$  is inversely proportional to  $n_{\text{H}}^2$  for a fixed ionization fraction (Equation 22), meaning that it is likely to be small except in low density regions. In our calculations, we find that the volume-weighted mean temperature  $\bar{T}_V \approx 290$  K exceeds the density-weighted value  $\bar{T}_M \approx 67$  K by more than a factor of 4. Similarly, the volume-weighted median  $T_{50,V} \approx 163$  K exceeds the mass-weighted median  $T_{50,M} \approx 35$  K by a similar value. This difference is particularly dramatic for the high-temperature tails of the distribution: while approximately 8% of the volume in our box has a  $T_{\text{eff}}$  greater than 1000 K, only 0.3% of the mass does.

We thus expect  $\text{CH}^+$  to mostly be found in low-density regions. We show in Figure 7 the regions of  $T - v_d$ ,  $T - n_{\text{H}}$ , and  $v_d - n_{\text{H}}$  phase space in which most of the  $\text{CH}^+$  mass is contained. For instance, in the middle panel, we have created  $256^2$  logarithmically-spaced bins spanning the full range of temperatures and densities found in the simulation output. The color scale shows the fraction of the total mass in each of these  $T - n_{\text{H}}$  bins, while the black contours show the regions of phase space that contain the top 99%, 90%, 50%, 10%, and 1% of the the  $\text{CH}^+$ . The left and right panels repeat this procedure for  $T - v_d$  and  $v_d - n_{\text{H}}$ , respectively. These plots

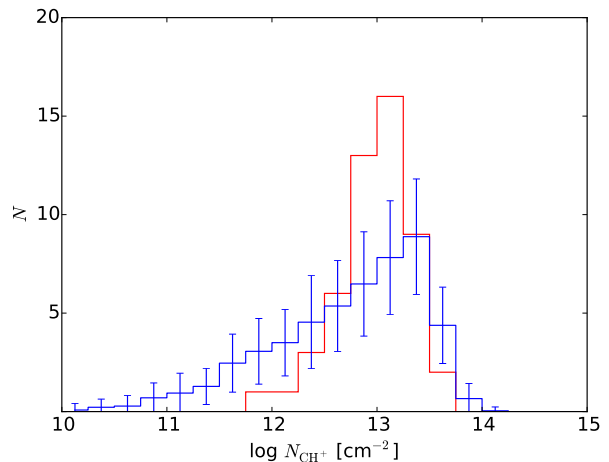


**Figure 8.** Blue - average histogram of  $\text{CH}^+$  column densities over 2500 lines of sight passing through the simulation volume. The error bars indicate the  $1 - \sigma$  range of variation over all 50 samples of 50 sight lines each. Red - histogram of the  $\text{CH}^+$  column densities from the 50 sight line sample in Weselak et al. (2008).

confirm our expectation that regions with  $T \gtrsim 1000$  K and  $v_d \gtrsim \sigma_{3D} \approx 4$  km  $\text{s}^{-1}$  tend to be found at low density, with typical values of  $n_{\text{H}} \sim$  a few H nuclei per  $\text{cm}^3$ . They also show that, while these regions are rare, they contain almost all of the  $\text{CH}^+$  molecules.

The middle panel of Figure 7 illustrates the importance of the intermittency in  $\Gamma_{\text{Turb}}$  in setting the gas temperature. The lower curve of this diagram traces out a line that corresponds to what the temperature as a function of density would be if we considered only  $\Gamma_{\text{PE}}$ ,  $\Gamma_{\text{CR}}$ , and the various cooling processes described in section 2.3. Most of the gas in the simulation receives little heating from turbulence dissipation and thus lies at or near this line. A small fraction of the gas, however, is heated to significantly higher temperatures by the effects of turbulence, and this gas comprises the bulk of the material that is heated above  $\sim 1000$  K. We find that without  $\Gamma_{\text{Turb}}$ , the fraction of mass in the simulation heated to  $T > 1000$  K would drop by approximately a factor of 20.

Sheffer et al. (2008), following Ritchey et al. (2006), used the ratio of  $N_{\text{CH}^+}$  to  $N_{\text{CH}}$  along with  $G_0$  and  $x(\text{H}_2)$  as an empirical probe of the gas density along a number of diffuse sight lines. The resulting density estimates were generally quite low, with typical  $n_{\text{H}} \sim 3$   $\text{cm}^{-3}$ , and in some cases much lower than estimates for  $n_{\text{H}}$  inferred from  $\text{C}^+$  excitation for the same sight lines (Sonnentrucker et al. 2002, 2003). Sheffer et al. (2008) interpret this as saying that a significant portion of the extinction and atomic hydrogen are associated with purely atomic regions that contain no  $\text{CH}^+$ , and that the corresponding increase in  $G_0$  increases the estimate for  $n_{\text{H}}$ . Our result suggests an alternative explanation: that the  $\text{CH}^+$  really is predominately found at low  $n_{\text{H}}$ , while the  $\text{C}^+$  observations are probing something closer to the mean density.

### 3.2 Sight-line Analysis

Weselak et al. (2008) presented a sample of 53  $\text{CH}^+$ -containing sight lines, 50 of which also had measurements of

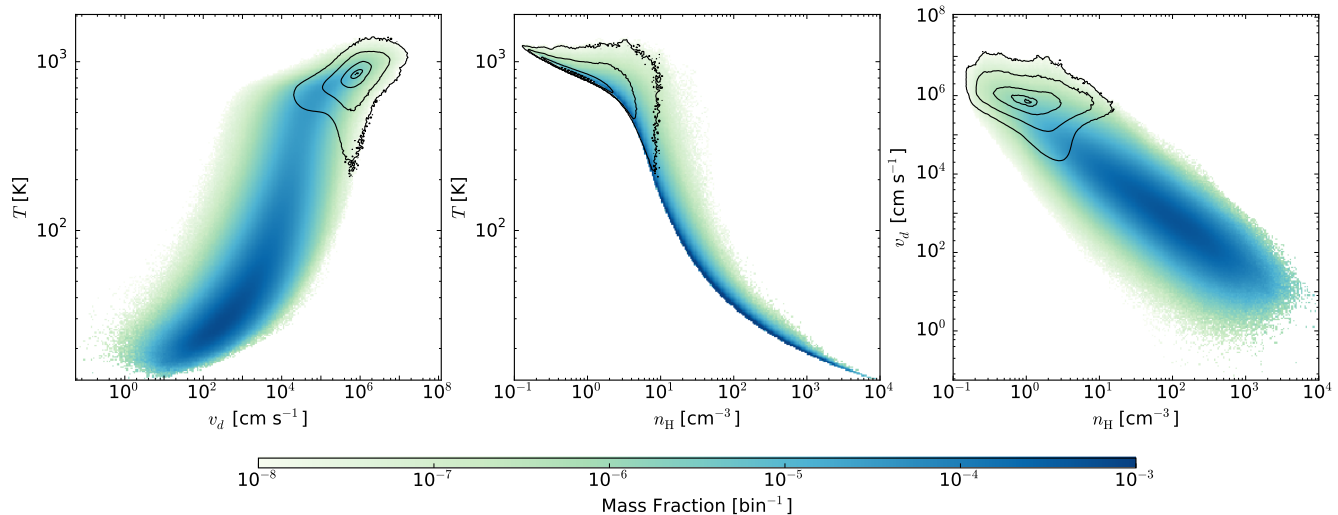


**Figure 7.** Left - the color scale shows the fraction of the total mass in each logarithmically-spaced  $T - v_d$  bin. The black contours show the region of phase space in which 99, 90, 50, 10, and 1 percent of the  $\text{CH}^+$  is found. Middle - same, but for  $T - n_{\text{H}}$ . Right - same, but for  $v_d - n_{\text{H}}$ .

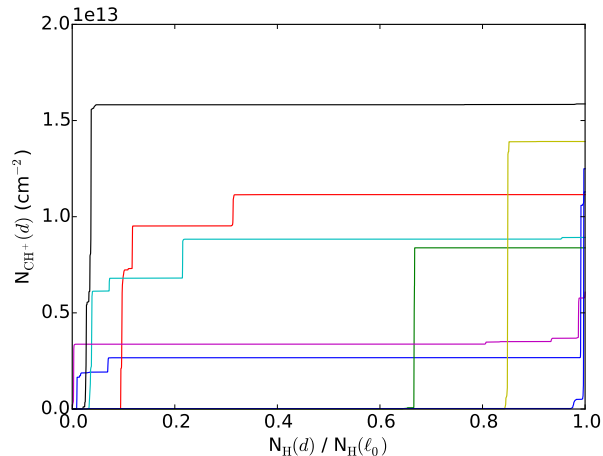


**Figure 9.**  $\text{CH}^+$  column density versus total column density  $N_{\text{H}}$  integrated along the same eight sight lines shown in Table 2. The quantities  $N_{\text{CH}^+}(d)$  and  $N_{\text{H}}(d)$  are the  $\text{CH}^+$  and total column densities integrated up through path length  $d$  along each ray. The  $x$ -axis has been normalized by the total column density  $N_{\text{H}}(\ell_0)$  to fit all the rays on the same plot.

$N_{\text{H}}$  and  $N_{\text{H}_2}$ . For the purpose of comparing with observations, we will adopt these 50 sight lines as our observational sample. We limit ourselves to this sample so that the  $\text{CH}^+$  column densities would all be calculated in a consistent way, but the distribution of columns in Weselak et al. (2008) is quite similar to that of Sheffer et al. (2008), which included both original data and results from many previous studies (Federman et al. 1997; Gredel 1997; Knauth et al. 2001; Pan et al. 2004).

Our model, by construction, has the same mean values of  $\bar{N}_{\text{H}}$  and  $\bar{N}_{\text{H}_2}$  as the Weselak et al. (2008) sample. The observed mean and median  $\text{CH}^+$  column densities for these sight lines are  $1.2 \times 10^{13} \text{ cm}^{-2}$  and  $1.1 \times 10^{13} \text{ cm}^{-2}$ , respectively. The corresponding values in our model are  $1.3 \times 10^{13} \text{ cm}^{-2}$  and  $8.1 \times 10^{12} \text{ cm}^{-2}$ , i.e. our mean is higher by 8% and

our median is lower by 26%. To further compare against the observational sample, we generate 2500 synthetic observations by casting 50 groups of 50 rays orthogonally through our computational domain as follows. For each ray, we randomly select one of the  $x$ ,  $y$ , and  $z$  directions, and then we randomly select a coordinate describing ray’s position in the corresponding normal plane. For example, for a ray aligned with the  $z$ -axis, we would randomly select a point in the  $xy$  plane from a uniform distribution to describe the position of the ray in the box. For each group of rays, we construct a histogram of  $N_{\text{CH}^+}$  using 20 bins spaced evenly of the range  $\log N_{\text{CH}^+} = 10$  to  $\log N_{\text{CH}^+} = 15$  and compare it against the corresponding histogram for the observational sample. The result is shown in Figure 8. The error bars indicate the  $1 - \sigma$  variation in the number of sight lines per bin. The number of groups was set at 50 because that number was sufficient for the error bars to be converged: the maximum change in the  $1 - \sigma$  error over all the bins was 15%, and the mean change was only 1%. We find that, while our model agrees well with the mean and median of the observational sample, it does tend to over-produce both very large and very small values. However, the sight lines in Weselak et al. (2008) do not constitute a truly random sampling in that they were chosen because  $\text{CH}^+$  lines were detectable and the H and  $\text{H}_2$  column densities were measurable. This is likely not the case for the very low column lines in our model.

From our sample of 2500 rays, we choose 8 “typical” sight lines for more detailed investigation as follows. First, we randomly draw a ray from the sample. Next, we keep it only if both  $N_{\text{CH}^+}$  and  $N_{\text{H}}$  are within 50% of the overall sample means. Otherwise, we throw it away and draw again. We stop when 8 rays have been selected. The properties of these sight lines are described in Table 2. Here, the notation  $\bar{x}_{99}$  means the average value of  $x$  in the cells that are in the top 99% of the  $\text{CH}^+$  number density distribution. Thus,  $\bar{n}_{\text{H},99}$ ,  $\bar{T}_{\text{M},99}$ , and  $\bar{v}_d,99$  are the mean density, mass-weighted temperature, and drift velocity in the regions which contain 99% of the  $\text{CH}^+$ . We find that, consistent with Figure 7,

almost all of the  $\text{CH}^+$  in these sight lines is found in low-density, high-temperature, high-drift pockets of gas, with typical values of  $\bar{n}_{\text{H},99} \approx 1 - 2 \text{ cm}^{-3}$ ,  $\bar{T}_{\text{M},99} \approx 700 \text{ K}$ , and  $\bar{v}_{d,99} \approx 2 - 3 \text{ km s}^{-1}$ . These temperatures and velocities are quite similar to those obtained in the TDR models of Godard, Falgarone & Pineau Des Forêts (2009) using very different techniques.

The “temperature”  $\mu_{\text{H}} v_d^2 / 3k$  associated with a  $4 \text{ km s}^{-1}$  drift velocity is  $\approx 900 \text{ K}$ , comparable to  $\bar{T}_{\text{M},99}$ . Both effects thus appear to be important for building up  $\text{CH}^+$  columns in excess of  $10^{13} \text{ cm}^{-2}$ . To gauge the relative importance of the two effects, we repeat our calculation with  $v_d$  computed as above, but with  $T$  fixed at  $35 \text{ K}$ . The result is that the mean  $\text{CH}^+$  column drops from  $\approx 1.3 \times 10^{13} \text{ cm}^{-2}$  to  $\approx 8.0 \times 10^{12} \text{ cm}^{-2}$ . If we repeat the same experiment with  $T$  computed as above, but ignoring the effects of  $v_d$ , the  $\text{CH}^+$  column drops dramatically, down to  $\approx 5.0 \times 10^{11} \text{ cm}^{-2}$ . Thus, the  $\text{CH}^+$  chemistry in our model appears to be mainly driven by ion-neutral drift, with the kinetic temperature making a secondary, but not negligible, contribution to the total column.

Finally, to gauge the spatial extent of these regions, we show in Figure 9 the result of integrating  $N_{\text{CH}^+}$  and  $N_{\text{H}}$  along each of the 8 rays in Table 2. All of the rays show the same general behavior: there are large regions that make basically no contribution to  $\text{CH}^+$  column, punctuated by a few thin zones where the  $\text{CH}^+$  abundance is substantial. The typical sight line intersects approximately 2-4 of these regions. This analysis further confirms the view of Falgarone & Puget (1995) - that the cold ISM contains isolated patches of hot, chemically active gas, and that these regions are crucial to understanding diffuse cloud chemistry.

The gas densities we infer for the  $\text{CH}^+$ -containing regions in our model are lower than those typically associated with gas containing substantial abundances of  $\text{H}_2$ . As discussed in Section 2.5, a substantial  $\text{H}_2$  fraction is crucial for  $\text{CH}^+$  formation, and our model suggests that low densities are crucial, as well. However, it is not only the local gas density that is important for setting the  $\text{H}_2$  fraction; the total shielding from the ambient radiation field matters as well. In PDR models that assume constant density, this distinction is not made, but in a supersonically turbulent medium, it is entirely possible for a region with a low local gas density to nonetheless be well-shielded from FUV radiation. Indeed, Table 2 and Figure 9 show that, in our model, the  $\text{CH}^+$ -forming regions tend to be randomly distributed along sight lines, so that many of them would be well-shielded enough ( $A_V$  greater than a few tenths) for molecules to form. That said, our adoption of a constant  $\text{H}_2$  fraction is clearly an idealization. A better approach would be to self-consistently simulate the formation and destruction of  $\text{H}_2$  in the numerical simulation assuming some illumination, so that the molecular fraction (as well as the ortho-to-para ratio) could be tracked.

### 3.3 $\text{H}_2$ Emission

At  $T \gtrsim 1000 \text{ K}$ , significant numbers of  $\text{H}_2$  molecules can be excited to  $J \geq 2$  rotational levels, producing observable emission in the  $J = 2 \rightarrow 0$ ,  $J = 3 \rightarrow 1$ , and  $J = 4 \rightarrow 2$  lines. This emission is known to be correlated with  $\text{CH}^+$  column density (Frisch & Jura 1980; Lambert &

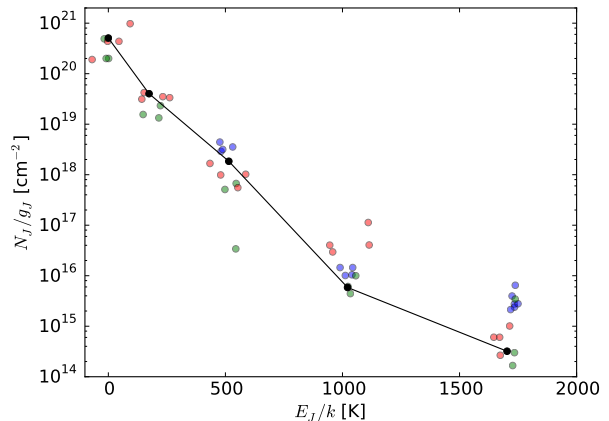


**Figure 10.** Excitation diagram for the first 5 rotational levels of  $\text{H}_2$  from our model compared to observed values. The  $y$ -axis shows the mean column densities in each rotational level divided by the degeneracy factors  $g_J$ . The  $x$ -axis is the energy of each level expressed as a temperature. Red circles - Lacour et al. (2005). Green circles - Gry et al. (2002). Blue circles - Ingalls et al. (2011). Black circles - our model. We have scaled the column densities up by a factor of 3 to match the mean  $\text{H}_2$  column density of the observations. The data have been shifted slightly along the  $x$ -axis for clarity.

Danks 1986; Jensen et al. 2010), and has been interpreted as observational evidence for the intermittent dissipation of MHD turbulence (Falgarone et al. 2005b). Because diffuse clouds are typically below the critical densities of the  $J = 3$  and higher lines, the level populations are in general non-thermal, and the level populations depend on both  $T$  and the gas density. Observations of  $\text{H}_2$  excitation can thus help to constrain the temperature and density structure in models of  $\text{CH}^+$  production in diffuse clouds. To compare our results against these observations, we calculate the  $\text{H}_2$  rotational level populations by balancing collisional excitation with collisional de-excitation and spontaneous emission for the first 20 rotational levels of  $\text{H}_2$ . We solve the resulting eigenvalue problem using SciPy’s `scipy.linalg.eig` routine. The full Cython<sup>2</sup> code used for this calculation, as well as the rest of the code used in this paper, is available at <https://bitbucket.org/atmyers/chplus>.

Observations of  $N_{\text{H}_2}(J = 0)$  and  $N_{\text{H}_2}(J = 1)$  indicate that ortho- (odd  $J$ ) and para- (even  $J$ ) hydrogen are not generally in found in the equilibrium 3:1 ratio in the ISM. For example, in the three sight lines presented in Gry et al. (2002),  $\gamma = N_{\text{H}_2}(J = 1)/N_{\text{H}_2}(J = 0)$  is 0.7, 0.6, and 0.4. Likewise, in the four lines from Lacour et al. (2005),  $\gamma = 0.3, 1.6, 0.6,$  and  $0.9$ . Nehmé et al. (2008) found  $\gamma = 0.7$  towards HD 102065, and Ingalls et al. (2011) found that this assumption fit their data for 6 nearby sight lines as well. In this paper, we will therefore fix the ortho:para ratio at 0.7 and treat ortho- $\text{H}_2$  and para- $\text{H}_2$  as separate species. For the energy levels  $E_J$ , we treat both forms of  $\text{H}_2$  as quantum rotors with rotational temperature  $T_r = 85.3 \text{ K}$ . We used the Einstein A coefficients from Wolniewicz, Simbotin & Dalgarno (1998) and the collisional excitation rates from Le Boulot,

<sup>2</sup> <http://cython.org/>

$N_{\text{CH}^+}$ ( $10^{13} \text{ cm}^{-2}$ )	$N_{\text{H}}$ ( $10^{21} \text{ cm}^{-2}$ )	$\bar{n}_{\text{H}}$ ( $\text{cm}^{-3}$ )	$\sigma_v$ ( $\text{km s}^{-1}$ )	$\bar{T}_{\text{M}}$ (K)	$\bar{n}_{\text{H},99}$ ( $\text{cm}^{-3}$ )	$\bar{T}_{\text{M},99}$ (K)	$\bar{v}_{d,99}$ ( $\text{km s}^{-1}$ )
1.1	2.2	36.0	1.8	60.0	1.5	713.0	2.1
0.8	2.2	36.8	1.2	59.5	1.6	710.9	3.0
1.1	1.2	19.8	1.9	92.5	1.7	708.5	2.3
0.9	1.3	21.4	2.2	85.4	1.4	713.0	2.2
0.6	1.9	31.2	2.2	69.3	1.9	682.3	1.7
1.4	2.0	32.4	0.7	61.0	1.3	715.2	2.5
1.6	1.9	31.7	1.8	66.9	1.9	676.6	2.2
1.2	2.7	43.4	0.8	51.0	1.3	715.2	1.9

**Table 2.** Data from 8 randomly selected rays cast through the problem domain. Column 1 - the CH<sup>+</sup> column density. Column 2 - the total column density. Column 3 - the mean number density. Column 4 - The 1D rms velocity dispersion. Column 5 - The mass-weighted mean temperature. Column 6 - The mean number density in the top 99% of cells by CH<sup>+</sup> number density. Column 7 - The mass-weighted mean temperature in that same subset of cells. Column 8 - The mean drift velocity in the same cells.

Pineau des Forêts & Flower (1999). The degeneracy factors are  $g_J = (2J + 1)$  (para) and  $g_J = 3(2J + 1)$  (ortho).

The result of this calculation for  $J = 0$  to 4 is shown in Figure 10, compared against the H<sub>2</sub> excitation observations from Gry et al. (2002), Lacour et al. (2005) and Ingalls et al. (2011). We have scaled all the column densities in our model up by a factor of 3 to match the mean H<sub>2</sub> column in the above papers. For all of the levels, our model result lies within the spread given by the observations. The mean  $J = 1$  to  $J = 0$  rotational temperature in our calculation, defined by

$$\frac{N_{\text{H}_2}(J=1)}{N_{\text{H}_2}(J=0)} = \exp \frac{-171 \text{ K}}{T_{10}}, \quad (30)$$

is  $\approx 67$  K, very close to the mean value for the sample of 38 sight lines in Rachford et al. (2009) based on FUSE measurements. Because there is a wide range of temperatures present and because the  $J = 2$  and higher lines are generally not in thermal equilibrium, however, our results for higher lines are not well-described by a single rotation temperature.

## 4 CONCLUSIONS

The intermittent dissipation of turbulence in the ISM has been proposed as an explanation for the high ( $> 10^{13} \text{ cm}^{-2}$ ) CH<sup>+</sup> column densities commonly observed along diffuse molecular sight lines (Falgarone, Pineau des Forêts & Roueff 1995). Turbulence can aid the production of CH<sup>+</sup> both by heating a small percentage of the gas directly (Lambert & Danks 1986; Falgarone, Pineau des Forêts & Roueff 1995; Pan & Padoan 2009) and by leading to large drift velocities (Spaans 1995; Federman et al. 1996; Sheffer et al. 2008) within localized regions of intense dissipation. Detailed dynamical and chemical models of these intense dissipation events have had much success in modeling the chemical properties of diffuse sight lines, although the rate of strain in the dissipation events and their frequency in the ISM were assumed, not self-consistently calculated (Joulain et al. 1998; Godard, Falgarone & Pineau Des Forêts 2009).

We have re-assessed the origin of the CH<sup>+</sup> observed in the diffuse ISM by post-processing a direct numerical simulation of MHD turbulence, thereby self-consistently deter-

mining the properties of the intermittent turbulence that produces the CH<sup>+</sup>. We adopted the standard linewidth-size relation for molecular gas and set the total column density of our simulation equal to the mean value for the observed sample that we compare with; the resulting magnetic field in our simulation  $\sim 5 \mu\text{G}$  is typical for interstellar gas with  $\bar{n}_{\text{H}} \lesssim 300 \text{ cm}^{-3}$ . We inferred that the density in our simulation is  $n_{\text{H}} \simeq 30 \text{ cm}^{-3}$ , which implies that the size of the simulated region is  $\ell_0 \approx 20 \text{ pc}$  and the velocity dispersion is  $\sigma_{1\text{D}} \approx 2.3 \text{ km s}^{-1}$ . Our approach provides the astrophysical framework in which the above models fit, and it corroborates their results in several ways. Specifically:

(i) We have solved an energy balance equation cell-by-cell for the temperature. While most of the mass in our cloud is cold ( $\lesssim 35 \text{ K}$ ), a small fraction ( $\lesssim 1\%$ ) of the mass has been heated to temperatures in excess of 1000 K.

(ii) Similarly, we have computed the drift velocity in our simulation using an approximate analytic expression. While on average the drift is negligible, in isolated regions it can reach values equal to or exceeding the large scale RMS gas velocity of  $\sim 4 \text{ km s}^{-1}$ .

(iii) Both of these effects combine to easily produce CH<sup>+</sup> column densities in excess of  $10^{13} \text{ cm}^{-2}$ . We find that overall, the drift is more important, in that it alone accounts for about 2/3 of the CH<sup>+</sup> in the box, but the contribution from the gas temperature is not negligible.

(iv) Our work highlights the importance of including density variations in physical and chemical models of the ISM. 90% of the CH<sup>+</sup> is found in cells with densities of  $\approx 4 \text{ cm}^{-3}$  or less – significantly lower than the mean value. These cells make up  $\approx 5\%$  of the volume and  $\approx 0.2\%$  of the mass in the simulation and have typical temperatures and drift velocities of  $\approx 700 - 800 \text{ K}$  and  $\approx 3 - 4 \text{ km s}^{-1}$ . These values are quite similar to the TDR models of Godard, Falgarone & Pineau Des Forêts (2009), despite the difference of our approaches.

(v) We have estimated the CH<sup>+</sup> column density through our model and compared the resulting distribution to the sample of sight lines presented in Weselak et al. (2008). Our mean CH<sup>+</sup> column of  $1.3 \times 10^{13} \text{ cm}^{-2}$  agrees very well with the Weselak et al. sample, although the median is lower by  $\approx 26\%$ .

(vi) Finally, we computed the expected H<sub>2</sub> rotational line

emission from these hot regions, and found that it is consistent with observations of diffuse molecular sight lines.

Finally, there are several caveats to our work that bear mentioning. The first, and probably most significant, is that our temperature and chemistry calculations were done purely in post-processing, taking the magnetic field, velocity, and density data from an isothermal MHD turbulent box. We cannot address whether or not our results would have been different had the temperature been computed self-consistently and allowed to affect the subsequent flow. We have also not self-consistently computed the H<sub>2</sub> fraction or the ortho-to-para ratio, instead using an average value inferred from observation. However, as chemical models of diffuse molecular gas frequently assume constant density, we believe that our approach is a valid first step towards a fully self-consistent turbulent chemistry calculation. A second, related caveat is that our results are tied to particular values of the sonic and Alfvénic Mach numbers that were used in the turbulence simulation. As discussed in Section 2.2, however, these dimensionless numbers correspond to reasonable choices for the cloud density ( $\bar{n}_H = 30 \text{ cm}^{-3}$ ), length scale ( $L = 20 \text{ pc}$ ), and velocity dispersion ( $\sigma_v = 2.3 \text{ km s}^{-1}$ ). Furthermore, our choices for the Mach numbers yield results for the mean temperature, CH<sup>+</sup> abundance, and H<sub>2</sub> emission lines that are consistent with observations of diffuse molecular regions. A priori, the input parameters needed to “predict” these observations could have been inconsistent with the typical properties of diffuse molecular gas, but we find that this is not the case. Third, we have used an approximate formula to estimate the ion-neutral drift velocity in the strongly-coupled regime (Section 2.4). While our formula has been calibrated against low-Mach number ( $\mathcal{M} \approx 3$ ), non-ideal MHD simulations, we have extrapolated these results into the high-Mach number ( $\mathcal{M} \approx 10$ ) regime, where they have not been directly verified. Doing so would require running non-ideal turbulence simulations with ambipolar diffusion in the high-Mach number, strongly coupled regime, which are not currently computationally feasible.

## ACKNOWLEDGMENTS

ATM wishes to thank the anonymous referee for a thoughtful report that improved this paper. Support for this research was provided by NASA through NASA ATP grants NNX09AK31G and NNX13AB84G (CFM and PSL), the NSF through grants AST-0908553 and AST-1211729 (ATM and CFM), and the US Department of Energy at the Lawrence Livermore National Laboratory under grant LLNL-B569409 (A.T.M.). This research was also supported by grants of high performance computing resources from the National Center of Supercomputing Application through grant TG-MCA00N020. We have used `yt`<sup>3</sup> (Turk et al. 2011) as well as the `SciPy`<sup>4</sup> family of Python libraries for data analysis and plotting. Our analysis and visualization scripts are available online at <https://bitbucket.org/atmyers/chplus>.

<sup>3</sup> <http://yt-project.org/>

<sup>4</sup> <http://www.scipy.org/>

## REFERENCES

- Bertoldi F., McKee C. F., 1992, *ApJ*, 395, 140  
 Coppola C. M., D’Introno R., Galli D., Tennyson J., Longo S., 2012, *ApJS*, 199, 16  
 Crane P., Lambert D. L., Sheffer Y., 1995, *ApJS*, 99, 107  
 Crutcher R. M., Wandelt B., Heiles C., Falgarone E., Troland T. H., 2010, *ApJ*, 725, 466  
 Dalgarno A., 2006, *Proceedings of the National Academy of Science*, 103, 12269  
 Draine B. T., 1980, *ApJ*, 241, 1021  
 Draine B. T., Katz N., 1986, *ApJ*, 310, 392  
 Duley W. W., Hartquist T. W., Sternberg A., Wagenblast R., Williams D. A., 1992, *MNRAS*, 255, 463  
 Elitzur M., Watson W. D., 1978, *ApJL*, 222, L141  
 Elitzur M., Watson W. D., 1980, *ApJ*, 236, 172  
 Falgarone E., Pineau des Forets G., Roueff E., 1995, *A&A*, 300, 870  
 Falgarone E., Puget J.-L., 1995, *A&A*, 293, 840  
 Falgarone E., Verstraete L., Pineau Des Forêts G., Hily-Blant P., 2005a, *A&A*, 433, 997  
 Falgarone E., Verstraete L., Pineau Des Forêts G., Hily-Blant P., 2005b, *A&A*, 433, 997  
 Federman S. R., Knauth D. C., Lambert D. L., Andersson B.-G., 1997, *ApJ*, 489, 758  
 Federman S. R., Rawlings J. M. C., Taylor S. D., Williams D. A., 1996, *MNRAS*, 279, L41  
 Flower D. R., Pineau des Forets G., Hartquist T. W., 1985, *MNRAS*, 216, 775  
 Frisch P. C., Jura M., 1980, *ApJ*, 242, 560  
 Glassgold A. E., Galli D., Padovani M., 2012, *ApJ*, 756, 157  
 Glover S. C. O., Abel T., 2008, *MNRAS*, 388, 1627  
 Godard B., Falgarone E., Pineau Des Forêts G., 2009, *A&A*, 495, 847  
 Goldsmith P. F., Velusamy T., Li D., Langer W. D., 2010, *ApJ*, 715, 1370  
 Gredel R., 1997, *A&A*, 320, 929  
 Gredel R., van Dishoeck E. F., Black J. H., 1993, *A&A*, 269, 477  
 Grenier I. A., Casandjian J.-M., Terrier R., 2005, *Science*, 307, 1292  
 Gry C., Boulanger F., Nehmé C., Pineau des Forêts G., Habart E., Falgarone E., 2002, *A&A*, 391, 675  
 Habing H. J., 1968, *Bulletin Astronomical Institute of the Netherlands*, 19, 421  
 Hollenbach D., McKee C. F., 1979, *ApJS*, 41, 555  
 Indrioli N., McCall B. J., 2012, *ApJ*, 745, 91  
 Ingalls J. G., Bania T. M., Boulanger F., Draine B. T., Falgarone E., Hily-Blant P., 2011, *ApJ*, 743, 174  
 Jensen A. G., Snow T. P., Sonneborn G., Rachford B. L., 2010, *ApJ*, 711, 1236  
 Jones E., Oliphant T., Peterson P., et al., 2001–, *SciPy: Open source scientific tools for Python*  
 Joulain K., Falgarone E., Pineau des Forets G., Flower D., 1998, *A&A*, 340, 241  
 Knauth D. C., Federman S. R., Pan K., Yan M., Lambert D. L., 2001, *ApJS*, 135, 201  
 Lacour S., Ziskin V., Hébrard G., Oliveira C., André M. K., Ferlet R., Vidal-Madjar A., 2005, *ApJ*, 627, 251  
 Lambert D. L., Danks A. C., 1986, *ApJ*, 303, 401  
 Landau L. D., Lifshitz E. M., 1959, *Fluid mechanics*

- Le Bourlot J., Pineau des Forêts G., Flower D. R., 1999, MNRAS , 305, 802
- Li P. S., Martin D. F., Klein R. I., McKee C. F., 2012, ApJ , 745, 139
- Li P. S., McKee C. F., Klein R. I., Fisher R. T., 2008, ApJ , 684, 380
- Li P. S., Myers A., McKee C. F., 2012, ApJ , 760, 33
- Mac Low M.-M., 1999, ApJ , 524, 169
- Mathis J. S., Mezger P. G., Panagia N., 1983, A&A , 128, 212
- McKee C. F., Li P. S., Klein R. I., 2010, ApJ , 720, 1612
- McKee C. F., Ostriker E. C., 2007, ARAA , 45, 565
- Nehmé C., Le Bourlot J., Boulanger F., Pineau Des Forêts G., Gry C., 2008, A&A , 483, 485
- Pan K., Federman S. R., Cunha K., Smith V. V., Welty D. E., 2004, ApJS , 151, 313
- Pan L., Padoan P., 2009, ApJ , 692, 594
- Rachford B. L. et al., 2009, ApJS , 180, 125
- Ritchey A. M., Martinez M., Pan K., Federman S. R., Lambert D. L., 2006, ApJ , 649, 788
- Shaw G., Ferland G. J., Srianand R., Abel N. P., van Hoof P. A. M., Stancil P. C., 2008, ApJ , 675, 405
- Sheffer Y., Rogers M., Federman S. R., Abel N. P., Gredel R., Lambert D. L., Shaw G., 2008, ApJ , 687, 1075
- Shu F. H., 1992, Physics of Astrophysics, Vol. II. University Science Books
- Snow T. P., McCall B. J., 2006, ARAA , 44, 367
- Sofia U. J., Lauroesch J. T., Meyer D. M., Cartledge S. I. B., 2004, ApJ , 605, 272
- Sofia U. J., Parvathi V. S., Babu B. R. S., Murthy J., 2011, AJ , 141, 22
- Sonnentrucker P., Friedman S. D., Welty D. E., York D. G., Snow T. P., 2002, ApJ , 576, 241
- Sonnentrucker P., Friedman S. D., Welty D. E., York D. G., Snow T. P., 2003, ApJ , 596, 350
- Spaans M., 1995, PhD thesis, PhD thesis. University of Leiden, Leiden, The Netherlands , (1995)
- Sternberg A., Dalgarno A., 1995, ApJS , 99, 565
- Stone J. M., Ostriker E. C., Gammie C. F., 1998, ApJL , 508, L99
- Turk M. J., Smith B. D., Oishi J. S., Skory S., Skillman S. W., Abel T., Norman M. L., 2011, ApJS , 192, 9
- van Dishoeck E. F., Black J. H., 1986, ApJS , 62, 109
- Weselak T., Galazutdinov G., Musaev F., Krelowski J., 2008, A&A , 479, 149
- Wolfire M. G., Hollenbach D., McKee C. F., 2010, ApJ , 716, 1191
- Wolfire M. G., McKee C. F., Hollenbach D., Tielens A. G. G. M., 2003, ApJ , 587, 278
- Wolniewicz L., Simbotin I., Dalgarno A., 1998, ApJS , 115, 293
- Zweibel E. G., Brandenburg A., 1997, ApJ , 478, 563